Applied Acoustics 73 (2012) 423–432

Contents lists available at SciVerse ScienceDirect

Applied Acoustics

journal homepage: www.elsevier.com/locate/apacoust

Technical Note

Real-time extended-field-of-view ultrasound based on a standard PC

Shuohe Zheng, Qinghua Huang*, Lianwen Jin, Gang Wei

School of Electronic and Information Engineering, South China University of Technology, Guangzhou, PR China
Guangdong Provincial Key Laboratory of Short-Range Wireless Detection and Communication, Guangzou, PR China

ARTICLE INFO

Article history:
Received 23 February 2011
Received in revised form 10 August 2011
Accepted 17 September 2011
Available online 20 November 2011

Keywords:
Images registration
Ultrasound
Extended field-of-view
Frame interval
Block selection

ABSTRACT

Extended field-of-view (EFOV) can acquire a full field of vision, which can help doctors to make more objective and accurate diagnosis. Current EFOV techniques suffer from the low computation speed due to the large amount of ultrasound data to be processed. This paper describes an efficient technique to register 2D multiframe ultrasound images and produce EFOV images with significantly reduced computation time based on a standard PC. For registration of any two adjacent images, we propose to select less image blocks which are regarded as the most valid blocks based on the importance of image content. In registration of a sequence of images, with an assumption that the moving direction and speed of the probe are nearly identical during the data collection, we estimate the moving speed of the probe at the beginning of data collection and ignore redundant image data by processing a smaller number of frames according to a frame interval. The experimental results show that the computation speed of our method is increased by 7–80 times in comparison with two traditional methods, and can accurately produce EFOV images in real-time.

1. Introduction

Ultrasound is an easy-to-use, inexpensive and real-time imaging tool with no ionizing radiation, and has been widely utilized in medical applications. It is valuable for diagnosis in many areas of the human body, such as heart, liver, obstetrics and neurovascular tissues [1]. However, the image field of view (FOV) is limited by the probe width and scanning angle such that the system cannot produce a full view of the whole anatomy, making the diagnosis inconvenient. Although 3D ultrasound imaging has been deeply researched and can extend the FOV, it is actually an imaging modality that requires complicated hardware development [2] and computationally intensive algorithms for volume reconstruction [3]. As an alternative to extend the FOV of ultrasound probe, ultrasound extended-FOV (EFOV) imaging technique was firstly proposed by Weng and Tirumalai [4]. In the EFOV technique, a sequence of original B-mode images was acquired during a real-time scanning, and then fused together using methods of image registration to provide a panoramic and more easily interpretable image. The accuracy of distance measurements obtained with the EFOV has been confirmed in [5,21], indicating that it is an accurate and reliable technology in real applications.

With the emergence of the EFOV, lots of applications have been developed with this technology. It can provide valuable additional information and better documentation of the superficial lesions [6]. In musculoskeletal imaging [7], the primary benefits of EFOV are measuring and displaying abnormalities (most often fluid collections or masses and extra-articular extremity abnormalities). Though EFOV imaging of the fetus is limited by fetal movements, a list of obstetrical applications using EFOV were proposed by Henrich et al. [8], including the imaging of placenta, fetus, uterine pathology and pelvic pathology. Besides, the EFOV techniques are playing important roles in the applications of abdominal examination [9,10], urethrography [11], breast imaging [12], and spinal tissues [13].

Current EFOV systems mainly include image registration, geometric image transformation, panoramic image construction, and image display [14]. Image registration is the core of EFOV techniques. Accurate registration of two adjacent images is required before image fusion. In the method proposed by Weng and Tirumalai [4], the current frame (called moving image) was divided into a grid of non-overlapping blocks. Each image block was matched to the previous frame (called fixed image) and the results were treated as local motion vectors. Then a least-squares optimization technique was used to derive the global motion from the large number of local motion vectors. Paying more attention to improving the imaging accuracy, an FFT-based technique [15] was developed to predict the relatively large rotation angle of two registered images before searching for the registration parameters.

However, a large amount of image data should be processed in current EFOV techniques to guarantee the imaging accuracy. In traditional EFOV systems [4,14], all image frames are used. Currently, an ultrasound system can produce 20–30 image frames per sec., and almost 160–300 frames can be obtained in a scanning of 8–10 s. As each image needs to be processed in existing EFOV systems, the large number of frames makes the computation quite

* Corresponding author.
E-mail address: qhhuang@scut.edu.cn (Q. Huang).

0003-682X/$ - see front matter © 2011 Elsevier Ltd. All rights reserved.
doi:10.1016/j.apacoust.2011.09.013

expensive, leading to a limitation to real-time applications. Though some additional hardware systems such as FPGA platforms [16] have been used for accelerating the registration process, the cost and complexity of ultrasound imaging machine are accordingly increased.

In this paper, we aim to provide a real-time EFOV imaging technique using a standard PC, improving the computational efficiency of image registration without loss of imaging accuracy. This paper is organized as follows. Section 2 gives technical details of image registration with carefully selected blocks. Section 3 describes a rapid method for registration of an image sequence. Experimental methods and results are presented in Section 4. Finally, we provide discussions and draw the conclusions.

2. Algorithm for image registration

In order to generate EFOV ultrasound, a number of continuously captured B-mode images are required to be registered together. This task starts from the basic registration procedure for any two adjacent images (called two-image registration). Given two adjacent images denoted as fixed and moving images, respectively, we aim to make use of a small number of image blocks which are able to represent the main features in B-mode images and can be helpful to improve the registration accuracy and computational efficiency. To determine the image blocks to be used, important features are first extracted from the moving image and then employed for evaluating the importance for each block. According to the importance scores assigned to the blocks, they are selected with a pre-set number. Subsequently, local motion vectors can be obtained by registration of each selected block in the fixed image. The global motion is finally derived from the local motions, yielding the spatial relationship between the two adjacent images.

2.1. Extraction of image features

Due to the presence of speckles in ultrasound images, the registration using raw images may not be adequately robust. Extraction of image features can help improve registration accuracy as suggested in [17], in which leading points were identified for registration of 3D ultrasound images. In our previous work [18,19], we tested different features (i.e. scale invariant features [20], gradient, and intensity) for registration of B-mode images. In this study, two simple image features (i.e. the magnitude of gradient and the intensity) are selected for fast computation. Both of the two features emphasize the properties of the underlying anatomy. The magnitude of gradient emphasizes the edges and textures, while the intensity distinguishes the pixels in terms of brightness. The weighted sum of the two features is used as an importance score denoting the importance of a pixel, defined as:

$$im(x,y) = int(x,y) + w \times gra(x,y), \tag{1}$$

where $int(x, y)$ and $gra(x, y)$ are the intensity and the magnitude of gradient for pixel (x, y), respectively, and w the weight for balancing the two features.

In our implementation, the gradient is calculated in the spatial domain with a Sobel mask (3×3 pixels). The horizontal and vertical masks are shown in Fig. 1. Let $gra_H(x, y)$ and $gra_V(x, y)$ denote the spatial convolution results of horizontal and vertical masks for pixel (x, y), respectively, $gra(x, y)$ is computed by:

$$gra(x,y) = \sqrt{gra_H^2(x,y) + gra_V^2(x,y)}. \tag{2}$$

All gradients in the image are normalized to a range of 0–255. Because the edges are often visually rich of information, we assign a larger value to w. In this study, w is set to 2.0. Once again, the weighted sums of all the pixels are normalized to a range of 0–255 and saved as a feature image. Feature images extracted from the fixed and moving images are called fixed feature image and moving feature image, respectively. As shown in Fig. 2, the edges in the raw image are emphasized in the feature image.

-1	0	1
-2	0	2
-1	0	1

(a)

-1	-2	-1
0	0	0
1	2	1

(b)

Fig. 1. Sobel mask for gradient computation in the spatial domain. (a) Horizontal mask, and (b) vertical mask.

2.2. Leading point selection

In the feature images, the value of a pixel denotes its importance. A pixel with larger value means that it is of more importance, often corresponding to strong visual features in the original image. To determine whether a feature point is important or not, we define a threshold, T_f. In the moving feature image, if a pixel is greater than T_f, it is regarded as a leading point and put into a set, LP:

$$LP = \{(x,y) | im(x,y) \geqslant T_f\}. \tag{3}$$

The value of T_f should be carefully set. For a larger value of T_f, the number of leading points may be insufficient for registration of images. On the contrary, the lower T_f may retain a portion of the leading points with less importance. In our implementation, the value of T_f is empirically set to be 36.

2.3. Selection of blocks

Before searching valid blocks, a region to be searched should be determined and denoted as R_b in this paper. It is obvious that the blocks should be locating in the overlapping area of the fixed and moving images. As the translation of adjacent images is relatively small, the overlapping area is approximately the whole image excluding the boundary. Moreover, the top part of the image is the skin of the tested tissue, which hardly varies during the scanning due to the pressure of the probe. Thus the information in these areas is useless for registration. Block selection in these areas should be avoided. Thus, R_b is the overlapping area without the top part containing skin tissues.

In the procedure of two-image registration, a number of small image blocks are chosen from the moving image and the registrations for the blocks are conducted on the fixed image. The overall registration result can be estimated based on the block registrations. It has been proved that the registration using multiple image blocks can lead to more robust results [4]. However, not all arbitrarily selected blocks can be used for the registration. If a block is full of noises or useless information (e.g. its intensities are all white or all black), it may result in an inaccurate block registration, hence decreasing the overall registration accuracy. In this study, we define the validity of a block according to the number of leading points contained. The definition can be explained by an assumption that a block's validity is positively proportional to the important features it contains. Because the important features can be extracted and denoted as the leading points as mentioned above, the validity of a block can be represented by the number of leading points it contains, which is named as importance score (S_i).

As shown in Fig. 3, the determination of valid blocks starts from leading point selection. Then we search in R_b in the moving image for the block containing the most leading points in the search range, which is defined as the most valid block. This block is accepted if its

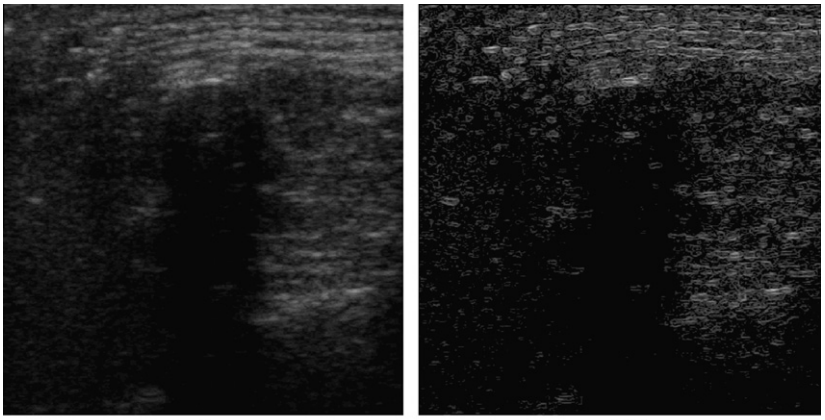

Fig. 2. An example for illustrating a raw ultrasound image and its feature image. (a) Raw image, and (b) its feature image.

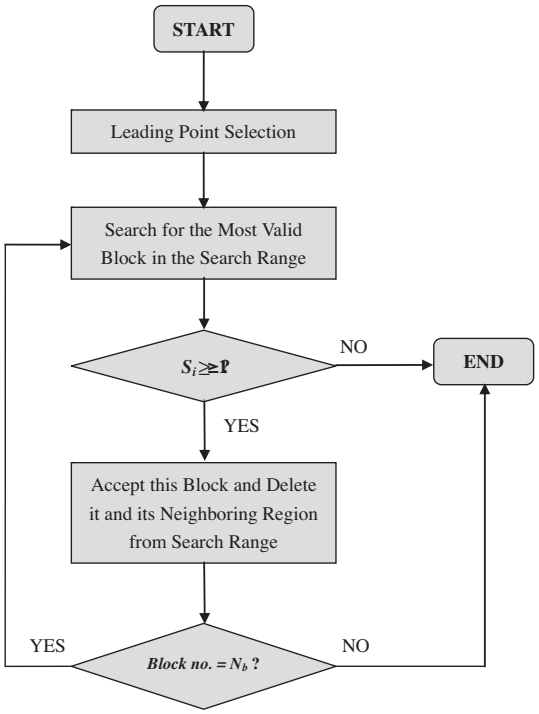

Fig. 3. A flowchart of the proposed block selection algorithm.

S_i is larger than 1; otherwise the selection of valid blocks is stopped. When the block is accepted, the block and its neighboring region (1.5 times the size of the block) are invalid for block searching, in order for selection of non-overlapping and less blocks. Block selection continues in the remaining valid region in R_b until the number of accepted blocks equals N_b. N_b can be set by users and is normally no less than 5. To achieve a good compromise between the computation efficiency and the registration accuracy, the block size is empirically set to be 32×32 in this study.

Fig. 4 illustrates a comparison of the block selection methods between Weng's method [4] and ours. It can be shown that our method selects a smaller number of blocks, all of which locate in the areas containing strong edges or rich textures.

2.4. Registration of the selected valid blocks

The valid blocks in S_b should be registered to the fixed image. Basically, the registration of a block from the moving image is to search for its best matching position in the fixed image. The sum of absolute difference (*SAD*) can evaluate the similarity between two blocks and is adopted in this study. The computation of *SAD* is expressed as follows:

$$SAD = \sum_x \sum_y |A(x,y) - B(x,y)|, \tag{4}$$

where A and B are two blocks to be matched, and (x, y) is the pixel index of the blocks.

In the practices of EFOV imaging, the probe is relatively slowly moved along the lateral direction, making the translation and rotation of each block on adjacent frames small. Hence, with an assumption that the rotation of each block can be ignored, the registration of each block can be based on a rigid transformation as shown below:

$$\begin{bmatrix} x' \\ y' \end{bmatrix} = \begin{bmatrix} x \\ y \end{bmatrix} + \begin{bmatrix} \Delta x \\ \Delta y \end{bmatrix}, \tag{5}$$

where (x, y) is the center of a block in the moving image, (x', y') is the center of the block that is registered in the fixed image, and $(\Delta x, \Delta y)$ is the translation of the block along the x and y directions. The aim of the block registration is to find $(\Delta x, \Delta y)$ which is regarded as a local motion vector corresponding to a specific valid block.

For a block (denoted as A) from the moving image, to find the block (denoted as B) with the best similarity in the fixed image requires a search procedure. Because the translation $(\Delta x, \Delta y)$ is relatively small, the search can be employed within a small search range (denoted as R_s) instead of the whole fixed image. The best matching block which has a minimum *SAD* with A can be found within the search range. In this study, R_s for B is set to be a rectangular region centered at the center of A, as illustrated in Fig. 5.

Due to the presence of tissue deformation caused by the probe and the tissue motions, however, the registrations of the blocks that locate in the relatively deformed areas may not be adequately accurate, hence introducing noises to the final image registration. Assuming that most of the block registration results are reliable, a noisy block registration can be identified if its result is significantly different from the others. We propose to use the following method to identify and exclude noisy registrations.

For N_b valid blocks, the average (A_r) and standard deviation (SD_r) of the N_b registration results are calculated. A_r is regarded as the expectation of the global motion. For every block registration $r(i)$, $i = 1, \ldots, N_b$, if the absolute difference between $r(i)$ and A_r is large than SD_r, the registration for the ith block is regarded as being inaccurate, and should be excluded. We deem that the registrations of

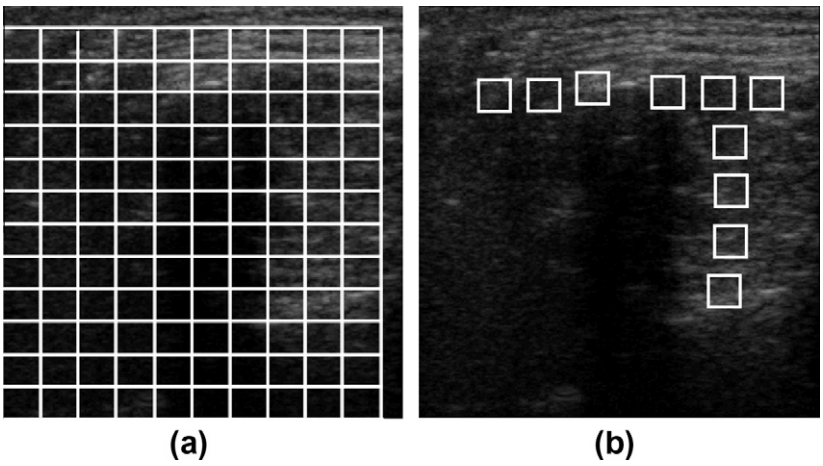

Fig. 4. An illustration showing the selection of blocks in (a) Weng's method, and (b) our method.

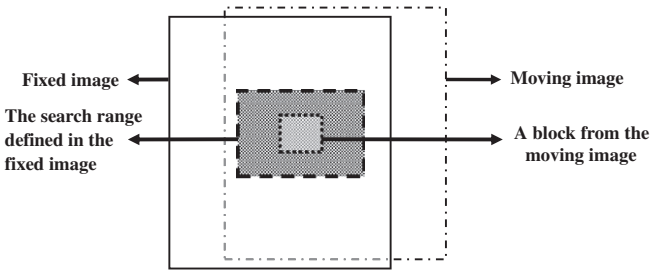

Fig. 5. A block from the moving image and its search range in the fixed image.

the remaining blocks are reliable for computing global registration result.

2.5. Global registration

Global motion should be found for the two-image registration. In EFOV ultrasound, the transformation of the two adjacent images is assumed to be rigid, including two translation variables (Δx_g and Δy_g) and one rotation variable (θ), as follows:

$$\begin{bmatrix} x' \\ y' \end{bmatrix} = \begin{bmatrix} \cos\theta & \sin\theta \\ -\sin\theta & \cos\theta \end{bmatrix} \begin{bmatrix} x \\ y \end{bmatrix} + \begin{bmatrix} \Delta x_g \\ \Delta y_g \end{bmatrix}, \tag{6}$$

where (x, y) and (x', y') are pixel locations in the moving and fixed images, respectively.

The global motion (Δx_g, Δy_g, θ) between the moving and fixed images can be derived from the local motions using the least-squares method [21]. In another words, the global motion can be obtained by minimizing the sum of all squared errors $E(\Delta x_g, \Delta y_g, \theta)$, as follows:

$$E = \sum_{i=1}^{n} \{[x'_i - \Delta x_g - (x_i \cos\theta - y_i \sin\theta)]^2 + [y'_i - \Delta y_g - (x_i \sin\theta + y_i \cos\theta)]^2, \tag{7}$$

where (x_i, y_i) and (x'_i, y'_i) are the centers of the ith block of the moving and fixed images, respectively. The minimum sum-of-squares error can be found by calculating the partial derivatives of $E(\Delta x_g, \Delta y_g, \theta)$:

$$\frac{\partial E}{\partial \theta} \equiv 0; \ \frac{\partial E}{\partial \Delta x_g} \equiv 0; \ \frac{\partial E}{\partial \Delta y_g} \equiv 0. \tag{8}$$

The solution of these equations is:

$$\theta = \tan^{-1}\left(\frac{\sum x_i \sum y'_i/n - \sum y_i \sum x'_i/n + \sum x'_i y_i - \sum x_i y'_i}{\sum x_i \sum x'_i/n + \sum y_i \sum y'_i/n - \sum x_i x'_i - \sum y_i y'_i}\right), \tag{9}$$

$$\begin{pmatrix} \Delta x_g \\ \Delta y_g \end{pmatrix} = \frac{1}{n}\left[\begin{pmatrix} \sum x'_i \\ \sum y'_i \end{pmatrix} - \begin{pmatrix} \cos\theta & -\sin\theta \\ \sin\theta & \cos\theta \end{pmatrix} \begin{pmatrix} \sum x_i \\ \sum y_i \end{pmatrix}\right], \tag{10}$$

where n is the total number of the blocks. Based on the estimated global motion, the moving image can be transformed into the coordinate system of the fixed image. The proposed algorithm is summarized in Fig. 6.

3. Methods for rapid EFOV

In order to produce EFOV ultrasound, a sequence of B-mode images is continuously captured and the method for two-image registration is performed on adjacent images. As mentioned above, the probe is moved slowly along the lateral direction during the real-time scanning, resulting in a large number of B-mode images and a large overlapping area between two adjacent images. Registering each pair of adjacent images is quite time-consuming. To improve the computation efficiency, we propose to sample the image frames based on a frame interval (*FI*) [18] which can be determined by estimating the moving speed of the probe. According to *FI*, the overlapping area and the search range (R_s) for the block registration can be determined. By significantly reducing the number of frames to be processed, the registration of the frame sequence can be conducted in a more rapid manner.

3.1. Estimation of the moving speed of the probe

With an assumption that the probe is moved along lateral direction and its moving speed is approximately invariant during the data collection, we can estimate the moving speed by registering the first $M + 1$ frames and averaging the translations for all pairs of adjacent frames, expressed as:

$$MRF = \frac{1}{M}\sum_{i=1}^{M} TOI_i, \tag{11}$$

where TOI_i is the lateral translation ratio between the $(i-1)$th and the ith frames, i.e. the percentage of the lateral translation with respect to the image width, and *MRF* the averaged translation ratio. The *MRF* can be approximately treated as the mean translation for adjacent frames in the whole sequence. The translations of these

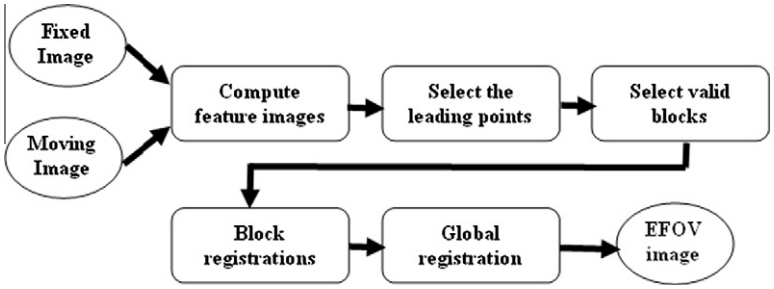

Fig. 6. The summarized method for rapidly producing EFOV ultrasound.

frames are relatively small and the overlapping area of adjacent frames is relatively large. Therefore, R_s in this procedure can be relatively small, and is of 56×42.

3.2. Estimation of the frame interval

In order for an accurate registration, a relatively large overlapping area of the moving and fixed images is required for accurate registration. Relatively large overlapping area indicates relatively small translation between adjacent frames. In free-hand scanning, the varying of the probe pressure and movement of the examined tissue are inevitable, so the image content should vary greatly for a pair of frames sampled using an *FI*. Thus, the *FI* should be carefully determined to avoid inaccurate registrations. In this study, three operators are recruited to perform the data collection in EFOV ultrasound. We empirically find that the overlapping area between two adjacent images should be no less than 80% of a single image. In other words, the maximum of the translation ratio between two adjacent images is 0.2. Accordingly, the *FI* used in this study is defined by:

$$FI = 0.2/MRF. \tag{12}$$

3.3. Registration of sampled frames

Having sampled the original frames, the remaining frames are put into a data set (denoted as *SF*), and used for frame sequence registration to obtain a larger EFOV ultrasound image. Because the number of frames to be processed is significantly reduced, the computation speed can be greatly improved. The translation ratio of any two adjacent sampled frames (*TEF*) is expressed as:

$$TEF = FI \times MRF. \tag{13}$$

As shown in Eq. (12), *TEF* is set to be 0.2 in this study. Therefore, the overlapping region between the fixed and the moving images is 80% of the area of an original B-mode image. Because the overlapping area is reduced and the image content appears to be more different for any two adjacent frames, R_s is accordingly increased to 120×50.

At the beginning of the frame sequence registration, the first two B-mode images in *SF* are regarded as the fixed image and the moving image, respectively. After the two images are registered and fused into a single image, the newly formed image is regarded as the fixed image and the third B-mode image in *SF* is chosen as the moving image. Then, the registration and fusion of the fixed and moving images repeats until all B-mode images in *SF* have been chosen. It is noted that the process of image fusion is realized by averaging any two pixels (from the fixed and moving images, respectively) at the same location in the overlapping area.

4. Experiments and results

4.1. Experimental methods

In the experiments, the computation time and the accuracy of the proposed method called rapid method in this paper are verified by comparing to two previously developed methods (i.e. Weng's method [4] and Chen's method [15]). To evaluate the computation efficiencies, two operators collect 4 data sets (denoted as A, B, C, and D, respectively, in this paper) from the arms and legs of a male subject and produce EFOV images using the three methods. The original data is collected from an ultrasound imaging machine (Sonix RP, Ultrasonix Medical Corp., Richmond, BC, Canada).

In Weng's and Chen's methods, every 4 images are selected for EFOV imaging. In our method, N_b is set to be 10 for the two-image registration and M is set to be 16 for estimation of the probe movement. All of the three methods are realized in a standard PC with a 3.0 GHz CPU and 2 GB RAM. The computation times using different methods for registrations of 10 pairs of randomly chosen adjacent frames and the overall image sequences are recorded for comparison purpose. In addition to the quantitative comparisons among previously reported EFOV algorithms, we compare the proposed method to a commercial ultrasound system (Model M5, Mindray company, Shenzhen, China) which offers EFOV imaging functions. The system is based on a laptop computer equipped with a 3.0 GHz CPU and 4 GB RAM. Because its probe is different from ours and its systematical time is unavailable, we can only make a rough comparison of the computation time between our method and the commercial system.

In addition, the imaging accuracy of our method is verified using 5 custom-designed phantoms, in each of which a plastic box with two sticks is used for distance measurement as illustrated

Fig. 7. A box with glass sticks carrying a piece of pork.

Table 1
Estimations of the moving speed and frame interval in our method.

Data set	Frame number	Moving speed (pixel/frame)	Frame interval
A (arm)	401	0.911	27
B (arm)	138	2.899	12
C (arm)	198	2.156	12
D (leg)	195	1.425	27

in Fig. 7. The diameter of each stick is 1.0 cm and the distance between the centers of the two sticks varies from 98.6 to 132.4 mm measured using a micrometer. Two operators scan each phantom twice to image the two sticks embedded in a piece of pork. The distances measured from the EFOV images produced by the three different methods can represent the imaging accuracies. Moreover, with reference to [22], Pearson's correlations (r), the level of significance of difference in measurement errors and intra-class correlation coefficient (ICC) of three methods are calculated for further evaluation of the proposed method.

4.2. Results

4.2.1. Comparisons of computational efficiency

The frame number, estimated speeds and frame intervals for the four data sets are shown in Table 1. For brevity, we give the EFOV images for data set C in Fig. 8. It can be seen that there is little difference among the EFOV images by qualitative comparisons, indicating good performance of the three methods in producing an

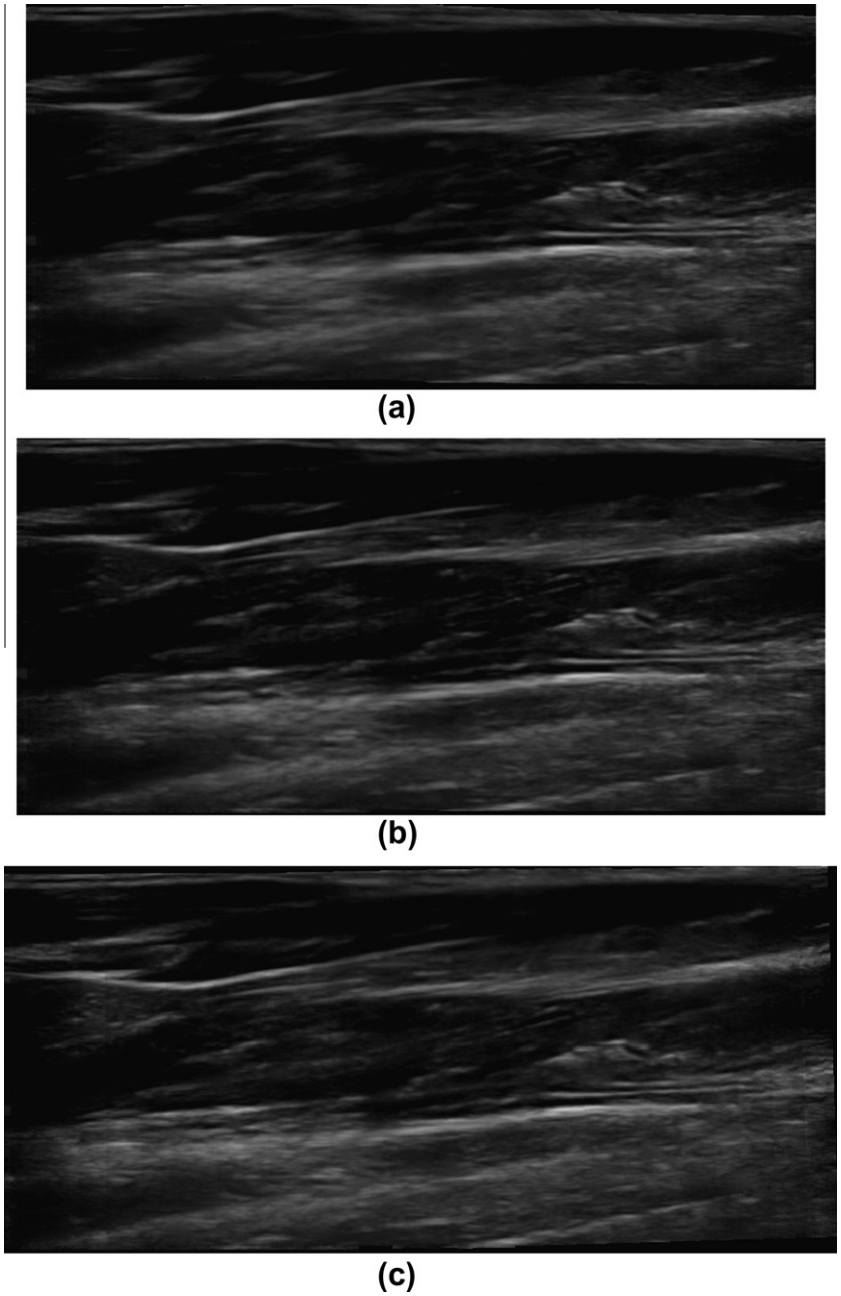

Fig. 8. The EFOV ultrasound images of data set C produced by (a) Weng's method, (b) Chen's method, and (c) our method. There are totally 198 original 2D ultrasound images collected from a subject's forearm.

Table 2
Computation times of different methods using data set A.

Method	Computation time of the registration (s)							
	10 randomly-chosen pairs of images					Mean	SD	Total
Weng's method	1.235	1.250	1.234	1.250	1.235	1.239	0.011	123.90
	1.234	1.250	1.235	1.219	1.234			
Chen's method	0.625	0.610	0.625	0.625	0.609	0.621	0.0069	62.155
	0.625	0.625	0.609	0.610	0.625			
Our method	0.094	0.110	0.156	0.141	0.156	0.144	0.026	2.894
	0.156	0.141	0.172	0.156	0.172			

Table 3
Computation times of different methods of data set B.

Method	Computation time of the registration (s)							
	10 randomly-chosen pairs of images					Mean	SD	Total
Weng's method	2.094	2.078	2.094	2.109	2.110	2.102	0.014	71.474
	2.125	2.141	2.110	2.094	2.078			
Chen's method	0.641	0.640	0.657	0.656	0.672	0.657	0.0085	22.342
	0.656	0.672	0.671	0.656	0.657			
Our method	0.110	0.110	0.187	0.203	0.204	0.182	0.051	2.926
	0.219	0.235	0.218	0.250	0.235			

Table 4
Computation times of different methods of data set C.

Method	Computation time of the registration (s)							
	10 randomly-chosen pairs of images					Mean	SD	Total
Weng's method	2.093	2.078	2.094	2.109	2.110	2.113	0.017	101.434
	2.109	2.094	2.125	2.125	2.141			
Chen's method	0.640	0.656	0.657	0.656	0.672	0.661	0.0086	31.735
	0.672	0.656	0.672	0.672	0.672			
Our method	0.125	0.110	0.109	0.172	0.171	0.161	0.028	3.388
	0.187	0.188	0.172	0.171	0.172			

Table 5
Computation times of different methods using data set D.

Method	Computation time of the registration (s)							
	10 randomly-chosen pairs of images					Mean	SD	Total
Weng's method	2.109	2.109	2.110	2.125	2.110	2.118	0.002	101.658
	2.156	2.125	2.109	2.125	2.110			
Chen's method	0.656	0.640	0.656	0.641	0.640	0.647	0.0078	31.077
	0.657	0.641	0.656	0.657	0.656			
Our method	0.062	0.078	0.062	0.141	0.140	0.112	0.040	1.343
	0.156	0.141	0.156	0.062	0.141			

ultrasound panorama. The computation times for the overall EFOV imaging and randomly chosen two-image registrations for the four data sets are presented in Tables 2–5, respectively. It is shown that our method computes an EFOV image in 1.3–3.4 s and can increase the computation speed by 7–80 times in comparison with the other two methods.

There are 198 original images collected in data set C, and our method takes 3.4 s. for computation of an EFOV image based on data set C. In contrast, the commercial system mentioned above takes around 12 s. to compute an EFOV image based on around 200 original images in the experiments, indicating that our method offers better computational efficiency. In summary, our method significantly outperforms the commercial system and the other two EFOV methods in terms of the computational efficiency.

4.2.2. Comparisons of imaging accuracy

Fig. 9 illustrates three typical EFOV images for one of the phantoms. The two sticks can be clearly seen and their centers can be easily marked. Table 6 shows the actual distance between the two sticks' centers of each phantom, and the distances measured by the two operators with respect to the EFOV images. The measurement error of Weng's method is $-0.33\% \pm 0.98\%$, that of our method is $-0.43\% \pm 1.29\%$, and that of Chen's method is $-12.45\% \pm 5.25\%$. Obviously, Weng's method offers the best accuracy. However, our method achieves an averaged measurement error which is slightly worse than Weng's method does and significantly better than Chen's method does.

Table 7 shows that all of the three methods demonstrate high correlations (i.e. Weng's: $r = 0.998$–0.999, $p < 0.05$; Chen's:

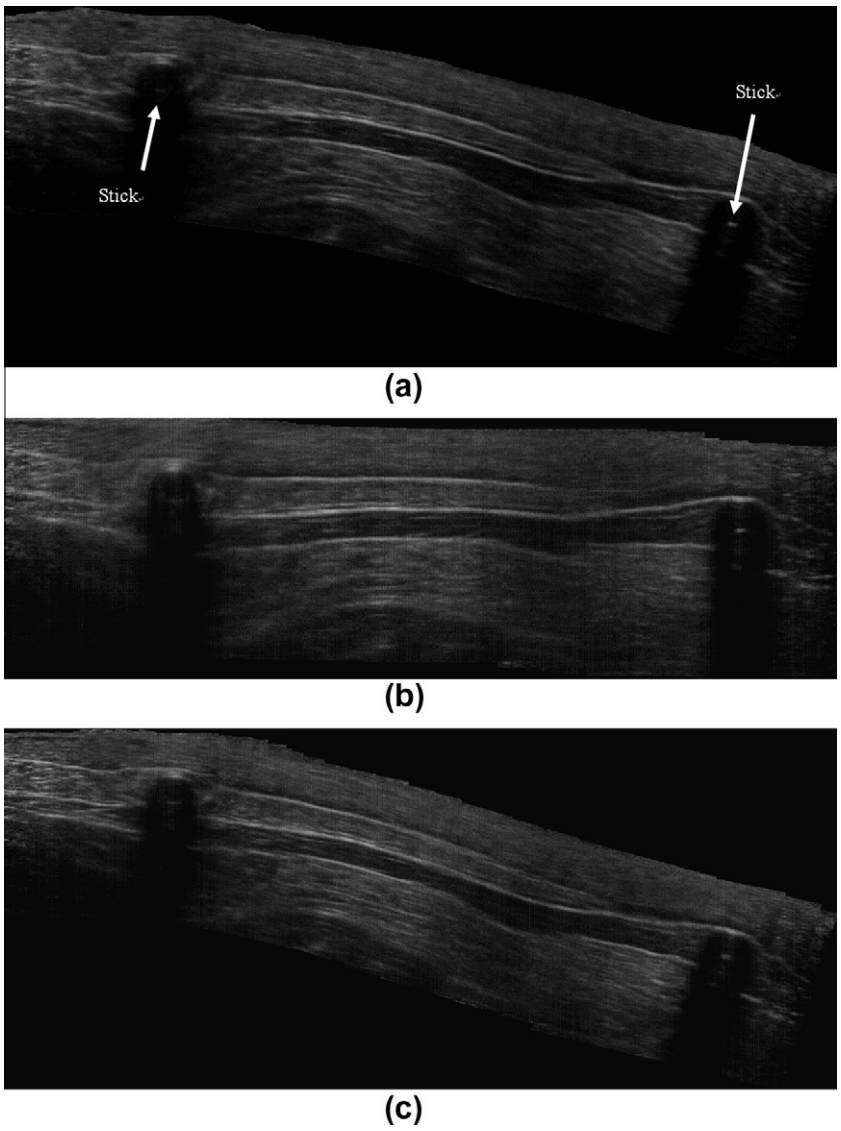

Fig. 9. Three EFOV images of a piece of pork with two sticks penetrated, produced by (a) Weng's method, (b) Chen's method, and (c) our method.

Table 6
The actual distance of 5 phantoms and the measured value of the two operators using three different EFOV methods.

	1st scan			2nd scan			
Phantom	Weng's method	Chen's method	Our method	Weng's method	Chen's method	Our method	Actual distance
Operator 1							
1	99.1	82.3	96.2	98.9	80.6	99.1	98.6
2	98.9	83.5	99.6	98.6	83.0	98.3	99.8
3	124.5	107.9	124.9	125.0	105.6	125.6	124.7
4	133.2	115.0	133.0	133.5	120.9	133.6	132.4
5	110.6	99.6	110.7	110.5	99.1	111.9	110.9
Operator 2							
1	95.6	88.2	95.1	96.2	88.5	95.8	98.6
2	98.9	78.5	98.4	99.6	79.1	99.0	99.8
3	125.1	108.9	125.5	124.9	108.9	124.9	124.7
4	132.5	129.9	132.1	133.0	129.8	132.0	132.4
5	110.3	99.8	110.3	110.7	102.4	111.8	110.9

$r = 0.957–0.985$, $p < 0.05$; and ours: $r = 0.998$, $p < 0.05$) between the actual and measured distance values. It can also be seen in Table 8 that Weng's and our methods have similar ICC values (i.e. 0.997 for Weng's method and 0.995 for ours), indicating a significantly low interobserver variability. In contrast, Chen's method (ICC = 0.670) shows a relatively poor reproducibility. Table 9 gives the evaluation results of repeatability with respect to the two scannings made by one operator. It is noted that the three methods all perform well in this experiment and achieve high repeatability (i.e. the ICC values vary from 0.982 to 1.0).

Table 7
The correlation of the measured values and actual values in three different EFOV methods.

Operators	EFOV methods	Pearson correlation coefficient (r)
Operator 1	Weng's method	0.999
	Chen's method	0.986
	Our method	0.998
Operator 2	Weng's method	0.998
	Chen's method	0.957
	Our method	0.998

Table 8
Interobserver variability (reproducibility) of three different EFOV methods in distance measurements.

EFOV methods	ICC values	Lower 95% CI	Upper 95% CI
Weng's method	0.997	0.989	0.999
Chen's method	0.670	−0.054	0.931
Our method	0.995	0.982	1.000

Table 9
Intraobserver variability (repeatability) of three different EFOV methods in distance measurements.

Operators	EFOV methods	ICC values	Lower 95% CI	Upper 95% CI
Operator 1	Weng's method	1.000	0.998	1.000
	Chen's method	0.982	0.839	0.998
	Our method	0.996	0.971	1.000
Operator 2	Weng's method	0.999	0.988	1.000
	Chen's method	0.998	0.985	1.000
	Our method	0.999	0.990	1.000

5. Discussions and conclusions

Ultrasound EFOV is a useful method for medical diagnosis. In this paper, we propose a rapid EFOV method. The computation speed and measurement accuracy are evaluated in the experiments. It can be seen from the Tables 2–5 that the average computational time for EFOV using our method has been significantly reduced in comparison with those of two previously used methods. Due to the use of Fourier transform, Chen's method is more computationally complicated than our method. Meanwhile, Weng's method selects more blocks in two-image registrations and processes all image frames, resulting in the longest computation time. In the comparisons of computation time, our method generates an EFOV image in a few seconds and increases the computation speed by approximately 7–80 times. Moreover, our system outperforms a commercial EFOV system, indicating that real-time EFOV imaging could be potentially realized using the proposed method.

It can be observed from the results of distance measurement that our method achieves the imaging results with an average error of less than 0.5%. Though the measurement accuracy achieved by our method is slightly lower than Weng's method, our method performs in a very rapid manner. In the measurement of correlation, all methods have a high correlation between the measured and actual distance values. It indicates that the custom-designed phantoms with different structures have little influence on the EFOV imaging results. For the evaluations of reproducibility and repeatability, the three methods all demonstrate good performance. In particular, Weng's and our methods present relatively high reproducibility and repeatability.

Nevertheless, there are two limitations to the implementation of the proposed method. First, we assume that the probe is linearly moved at an approximately uniform moving speed in this study. However, the movement of the probe may not always conform to this assumption. If this assumption cannot be satisfied (e.g. there are relatively large rotations of the probe during the scanning), the moving speed may be wrongly estimated and the EFOV images may be incorrectly produced. In state-of-the-art EFOV systems, currently used techniques cannot well deal with the movement of probe with an arbitrary trajectory. Basically, inaccurate image registration resulting from relatively large rotations of probe remains unsolved in existing EFOV systems. Second, it is well known that tissue deformation caused by the probe pressure is inevitable during the scanning. Due to the frame interval used in our method, two sampled frames to be registered may be collected with a relatively large time interval and under different pressure conditions; hence the same tissues appearing in the two images may be visually different in shape and/or size. Therefore, large registration errors may be resulted in, and have occurred in our experiments when comparing to Weng's method. Accordingly, research on detection of the probe movement and compensation of tissue deformations should be investigated in our future work.

In conclusion, we have developed an efficient technique for rapid registration of a sequence of B-mode images and generation of EFOV ultrasound images in real-time. To improve the efficiency of the two-image registration, we propose a new method to evaluate the validity of blocks and select a subset of blocks according to their importance scores. A small number of blocks with the best scores are used for the registration, hence increasing both of the registration accuracy and the computation speed. To further improve the computational efficiency, the proposed method for registration of a sequence of images makes use of a smaller number of ultrasound images sampled from the image sequence. The experimental results demonstrate that our method can significantly improve the computation efficiency without loss of imaging accuracy. It can be expected that, based on our method, real-time ultrasound EFOV can be realized and used in various clinical applications.

Acknowledgements

This work is supported by the Program for New Century Excellent Talents in University, Ministry of Education, China (No. NCET-10-0363), the Fundamental Research Funds for the Central Universities, SCUT (No. 2009ZM0059) and National Natural Science Funds of China (Nos. 61001181, 60902035 and 61075021). The authors would like to thank the two anonymous reviewers for their constructive comments.

References

[1] Beutel J, Kim Y, Horii SC. Handbook of medical imaging: display and PACS. SPIE Press; 2000.
[2] Dai YK, Tian J, Dong D, Yan GR, Zheng HR. Real-time visualized freehand 3D ultrasound reconstruction based on GPU. IEEE Trans Inf Technol Biomed 2010;14:1338–45.
[3] Huang QH, Lu MH, Zheng YP, Chi ZR. Speckle suppression and contrast enhancement in reconstruction of freehand 3D ultrasound images using an adaptive distance-weighted method. Appl Acoust 2009;70:21–30.
[4] Weng L, Tirumalai AP. US extended-field-of-view imaging technology. Radiology 1997;203:877–80.
[5] Fornage BD, Atkinson EN, Nock LF, Jones PH. US with extended field of view: phantom-tested accuracy of distance measurements. Radiology 2000;214:579–84.
[6] Yerli H, Eksioglu SY. Extended field-of-view sonography: evaluation of the superficial lesions. Can Assoc Radiol J 2009;60:35–9.
[7] Lin EC, Middleton WD, Teefey SA. Extended field of view sonography in musculoskeletal imaging. J Ultrasound Med 1999;18:147–52.
[8] Henrich W, Schmider A, Kjos S, Tutschek B, Dudenhausen JW. Advantages of and applications for extended field-of-view ultrasound in obstetrics. Arch Gynecol Obstet 2003;268:121–7.
[9] Kim SH, Choi BI, Kim KW, Lee KH, Han JK. Extended field-of-view sonography – advantages in abdominal applications. J Ultrasound Med 2003;22:385–94.
[10] Krombach GA, Truong S, Staatz G, Mahnken A, Prescher A, Tacke J, et al. Extended field-of-view sonography of the abdominal wall for delineation of the anatomy and diagnosis of abdominal wall defects. Rofo-Fortschr Rontg 2001;173:714–9.

[11] Mitterberger M, Christian G, Pinggera GM, Bartsch G, Strasser H, Pallwein L, et al. Gray scale and color Doppler sonography with extended field of view technique for the diagnostic evaluation of anterior urethral strictures. J Urology 2007;177:992–6.
[12] Weinstein SP, Conant EF, Sehgal C. Technical advances in breast ultrasound imaging. Semin Ultrasound CT MRI 2006;27:273–83.
[13] Staatz G, Hubner D, Wildberger JE, Gunther RW. Panoramic ultrasound of the spinal canal with determination of the conus medullaris level in neonates and young infants. Rofo-Fortschr Rontg 1999;170:564–7.
[14] Tirumalai A, Weng L, Grassmann A, Li M, Marquis S, Sutcliffe P, et al. New ultrasound image display with extended field of view. Proc Soc Photo-Opt Ins 1997;3031:409–19.
[15] Chen YL, Gao SK. Extended field-of-view ultrasound imaging technology for large-revolving-angle images. J Tsinghua Univ Sci Technol 2009;3:424–7.
[16] Dandekar O, Shekhar R. FPGA-Accelerated deformable image registration for improved target-delineation during CT-guided interventions. IEEE Trans Biomed Circuits Syst 2007;1:116–27.
[17] Foroughi P, Abolmaesumi P, Hashtrudi-Zaad K. Intra-subject elastic registration of 3D ultrasound images. Med Image Anal 2006;10:713–25.
[18] Zheng SH, Huang QH, Lu MH, Jin LW, Wang TF. Rapid image registration for extended-field-of-view ultrasound. In: Proceeding of the 4th international conference on bioinformatics and biomedical engineering; 2010.
[19] Kong LY, Huang QH, Lu MH, Zheng SH, Jin LW, Chen SP. Accurate image registration using SIFT for extended-field-of-view sonography. In: Proceeding of the 4th international conference on bioinformatics and biomedical engineering; 2010.
[20] Lowe DG. Object recognition from local scale-invariant features. In: Proceedings of the 7th IEEE international conference on computer vision; 1999. p. 1150–57.
[21] Althof RJ, Wind MGJ, Dobbins JT. A rapid and automatic image registration algorithm with subpixel accuracy. IEEE Trans Med Imaging 1997;16:308–16.
[22] Ying M, Sin MH. Comparison of extended field of view and dual image ultrasound techniques: accuracy and reliability of distance measurements in phantom study. Ultrasound Med Bio 2005;31:79–83.